

A minimal phase-field crystal modeling of vapor-liquid-solid coexistence and transitions

Zi-Le Wang,¹ Zhirong Liu,^{2,*} Zhi-Feng Huang,^{3,†} and Wenhui Duan^{1,4,5,6,‡}

¹State Key Laboratory of Low Dimensional Quantum Physics,
Department of Physics, Tsinghua University, Beijing 100084, China

²College of Chemistry and Molecular Engineering,

and Beijing National Laboratory for Molecular Sciences (BNLMS), Peking University, Beijing 100871, China

³Department of Physics and Astronomy, Wayne State University, Detroit, Michigan 48201, USA

⁴Institute for Advanced Study, Tsinghua University, Beijing 100084, China

⁵Collaborative Innovation Center of Quantum Matter, Tsinghua University, Beijing 100084, China

⁶Frontier Science Center for Quantum Information, Beijing 100084, China

(Dated: July 1, 2020)

A new phase field crystal model based on the density-field approach incorporating high-order correlations is developed to study vapor-liquid-solid coexistence and transitions. Conditions for the realization of phase coexistence and transition sequence are systematically analyzed, and shown to be satisfied by a broad range of model parameters, demonstrating the high flexibility and applicability of the model. Both temperature-density and temperature-pressure phase diagrams are identified, while structural evolution and coexistence among the three phases are examined through dynamical simulations. The model is also able to produce some temperature and pressure related material properties, including effects of thermal expansion and pressure on equilibrium lattice spacing, and temperature dependence of saturation vapor pressure. This model can be used as an effective approach for investigating a variety of material growth and deposition processes based on vapor-solid, liquid-solid, and vapor-liquid-solid growth.

I. INTRODUCTION

The vapor-based growth techniques, such as chemical vapor deposition (CVD), vapor-phase epitaxy (VPE), physical vapor deposition (PVD), and vapor-liquid-solid (VLS) growth, have been widely adopted in the fabrication and synthesis of two-dimensional (2D) and three-dimensional (3D) thin film materials^{1–3}, heterostructures^{4,5}, and nanowires^{6,7}. The interaction between vapor and solid or liquid phases plays an important role during the growth process since it determines the interfacial morphology and microstructures (including the formation of topological defects such as dislocations and grain boundaries) which affect the mechanical, electrical, magnetic, and thermal properties of the sample. A comprehensive understanding of the detailed dynamical process and underlying mechanisms, which are key in achieving high-quality material systems, is a challenging task for both experimental *in situ* studies and computer simulations given the multiple spatial and temporal scales involved. Both atomistic and coarse-grained modeling and simulation methods have been developed and applied to the study of these complex growth dynamics and mechanisms. For example, molecular dynamics simulations can probe into atomic-level microstructural details of the CVD^{8,9} and VLS^{10,11} growth processes. However, they are usually limited by the small simulation time scales (around ns to μ s) and system sizes that are far from reaching those of real experimental systems. Another widely used modeling technique is the phase field method^{12–14}, which is a coarse-grained, mesoscale approach at the long-wavelength limit, with the capability of describing system evolution on diffusion time

scales including that of interfacial morphology in CVD and VLS growth^{15–18}. Despite its advantage on accessing large length and time scales, phase field models are short of the description of short-wavelength, microscopic scales such as crystalline details and defect microstructures, and need to incorporate additional elastic, plastic, or orientation fields to account for the effects of elastoplasticity, defects, and multiple grain orientations.

Given its unique capacity in combining atomic-scale spatial resolution with diffusive time-scale dynamics and its intrinsic incorporation of elastoplasticity and multiple orientations, the phase field crystal (PFC) method^{19–21} has been developed rapidly in recent years as a useful tool in studying a wide range of phenomena of materials growth, structural evolution, and transformation. Its applications involve many important physical processes such as solidification^{20–24}, thin film epitaxy^{25,26}, crystal growth^{27,28}, dynamics of dislocations^{29–33} and grain boundaries^{34–37}, and the formation of quasicrystals^{38,39} and heterostructures⁴⁰. Most of early PFC models were constructed based on two-point correlation to describe systems governed by isotropic interactions²¹, where the crystal structures and ordered patterns are controlled by microscopic lattice length scales^{41–45}. Limited work has been attempted to explore the influence of orientation-dependent interactions and higher-order correlations^{46–48}. Recently, we have developed an angle-adjustable PFC formulation to provide a complete and concise way to incorporate any n -point correlations for modeling crystalline systems that are rotationally invariant and governed by both isotropic and anisotropic interparticle interactions⁴⁹. From this approach various 3D and 2D crystalline structures (such as bcc, simple

cubic, diamond cubic, simple monoclinic, orthorhombic, hexagonal, rhombic, and square phases) have been simulated. Such a complete density-field formulation further expands the scope of PFC models in the study of a variety of complex phase behaviors, and will be the basis of model development in this work.

Another limitation of most PFC models is that the modeling is usually restricted to liquid and solid phases and the related transition processes, but not involving vapor phase and its coupling or coexistence with solid or liquid state that are essential in simulating the widely used growth processes (e.g., CVD, VPE, PVD, and VLS growth) for the synthesis of thin films and nanostructures. Schwabach *et al.* made the first attempt to incorporate vapor phase into the PFC method⁵⁰, which requires an extra order parameter field (in addition to the PFC density field) in the free energy functional to generate realistic liquid-vapor and vapor-solid interfacial properties and step-flow growth. By assuming the long-wavelength approximation of three- and four-point correlations, Kocher and Provatas developed another PFC model with the use of a single PFC density field to effectively model vapor-liquid-solid transitions and simulate the growth processes involving two or three phases⁵¹.

In this paper we present a new and efficient vapor-liquid-solid PFC model based on the general density-field approach, with the expansion of three- and four-point direct correlations in terms of gradient nonlinearities in the free energy functional. The model efficiency can be viewed from its relatively simple form, serving as a minimal theory for modeling vapor-liquid-solid coexistence and transitions, and also from its tunability in achieving three-phase coexistence and the desired transition sequence across a broad range of model parameter values. The conditions and properties of these phase coexistence and transitions are calculated analytically and numerically, and verified through 2D dynamical simulations. In addition, we demonstrate the ability of this model in obtaining realistic material properties of, e.g., saturation vapor pressure, thermal expansion and pressure-induced contraction of crystalline lattice spacing which are absent in the existing PFC models. Since this model is built on the density-field formulation of Ref.⁴⁹ with a universal formalism for the expansion of any n -point correlations satisfying the condition of rotational invariance, it can be readily extended to incorporate bond-angle dependent anisotropic interactions (as in Ref.⁴⁹) into the three-phase formulation constructed here, to simulate a broader category of material systems.

II. MODEL

In the original PFC model, the free energy functional is given by^{19–21}

$$\mathcal{F}[n(\mathbf{r})] = \int d\mathbf{r} \left[-\frac{n}{2} (C_0 + C_2 \nabla^2 + C_4 \nabla^4) n - \frac{E_0}{4!} n^4 \right], \quad (1)$$

where $n(\mathbf{r})$ denotes the order parameter field of atomic number density variation, and the parameters C_0 , C_2 and C_4 can be connected to the two-point direct correlation function in classical density functional theory²¹. To enable the description of a spatially periodic, crystalline phase, $C_2 < 0$ and $C_4 < 0$ are required. Also $E_0 < 0$ is needed to prevent the divergence of density fluctuation. Via rescaling the length and time scales²⁰, Eq. (1) can be converted into the simplest form of

$$\mathcal{F}[n(\mathbf{r})] = \int d\mathbf{r} \left\{ \frac{1}{2} n [-\epsilon + (\nabla^2 + 1)^2] n + \frac{1}{4} n^4 \right\}, \quad (2)$$

where the only remaining parameter ϵ reflects the influence of the temperature. The larger the ϵ value, the lower the temperature it corresponds to.

The original PFC Eq. (2) contains only two-point direct correlation and excludes proper vapor-liquid-solid transitions. To incorporate the contributions from three- and four-point correlations, we adopt the general density-field approach developed in Ref.⁴⁹ which formulates the condition of rotational invariance in the expansion of any order of direct correlation functions, and consider the following minimal model

$$\begin{aligned} \mathcal{F}[n(\mathbf{r})] = & - \int B_0 n(\mathbf{r}) d\mathbf{r} \\ & - \frac{1}{2} \int n(\mathbf{r}) (C_0 + C_2 \nabla^2 + C_4 \nabla^4 + C_6 \nabla^6) n(\mathbf{r}) d\mathbf{r} \\ & - \frac{1}{3!} \int [D_0 n^3(\mathbf{r}) + D_{11} n^2(\mathbf{r}) \nabla^2 n(\mathbf{r})] d\mathbf{r} \\ & - \frac{1}{4!} \int \left\{ E_0 n^4(\mathbf{r}) + E_{1122} n^2(\mathbf{r}) [\nabla^2 n(\mathbf{r})]^2 \right\} d\mathbf{r}, \quad (3) \end{aligned}$$

where $E_0 < 0$ and $E_{1122} \leq 0$. The linear term with coefficient B_0 was usually ignored in most PFC studies since its integration over space gives a constant proportional to the average density \bar{n} and thus does not change the relative stability among different phases and the system dynamics. However, it was demonstrated recently that this term is crucial for the calculation and control of system pressure and elastic constants⁵². As will be shown below, B_0 should be temperature dependent to give a correct behavior of saturation vapor pressure. In this model parameters C_0 , C_2 , and C_4 also depend on temperature. Terms $D_{11} n^2 \nabla^2 n$ and $E_{1122} n^2 (\nabla^2 n)^2$, corresponding to the contributions from three- and four-point correlation respectively, are the main new components of our model and are key to achieve the coexistence and transitions between vapor, liquid, and solid phases, as will be proved both analytically and numerically in the next sections.

A negative E_{1122} is required in the presence of D_{11} to prevent the free-energy divergence of ordered phases, as will be explained in Sec. III B. In addition, the C_6 term is introduced to better control the crystalline modes in the presence of those two new nonlinear gradient terms, but not essential for obtaining the vapor-liquid-solid transitions. It is important to note that different from previous PFC models^{20,21,44,45}, here contributions from two-point correlation alone [i.e., $C_{j=0,2,4,6}$ terms in Eq. (3)] are not enough to determine even the lowest-order structural properties, and the three- and four-body interactions play an important role as can be seen in, e.g., the corresponding homogeneous-state structure factor derived in Appendix A.

Although in principle more higher-order rotationally invariant terms from three- and four-point correlations can be introduced through the formulation of Ref.⁴⁹, Eq. (3) is sufficient to produce vapor-liquid-solid transitions and serves as the corresponding minimal PFC model when considering only isotropic interactions. This model is convenient to be implemented, analyzed, and extended, with an important feature being that the coexistence of three phases and the triple point can be realized across a relatively broad range of parameters, as will be demonstrated below. It is of simpler form as compared to the previous two versions of PFC models incorporating vapor-liquid-solid phases, including that of Ref.⁵⁰ where an additional order parameter field and the associated free energy functional were needed for the control of vapor phase, and Ref.⁵¹ which also made use of three- and four-point direct correlation functions, while assuming them as products of Gaussian-type functions in Fourier space that correspond to infinite series of nonlinear gradient terms in real space. Detailed analyses of our model are given in the next section.

III. ANALYSIS OF VAPOR-LIQUID-SOLID TRANSITIONS

A. Vapor-liquid coexistence

Both vapor and liquid are uniform phases with $n(\mathbf{r}) = \bar{n}$, where \bar{n} is the average density variation of the system. Substituting it into Eq. (3) yields a simple Landau free energy per volume

$$f_u(\bar{n}) = -B_0\bar{n} - \frac{1}{2}C_0\bar{n}^2 - \frac{1}{6}D_0\bar{n}^3 - \frac{1}{24}E_0\bar{n}^4, \quad (4)$$

with a single variable \bar{n} .

In the rescaled original PFC model Eq. (2), we have $B_0 = D_0 = 0$, $C_0 = \epsilon - 1$, and the temperature-related parameter ϵ is usually assumed to be small^{20,21}. In that case, the $f_u(\bar{n})$ curve is convex, and thus there exists only one single phase under any density or pressure. In other words, vapor-liquid coexistence is absent under small ϵ . However, when we extend the parameter region to large ϵ , vapor-liquid coexistence actually occurs based on Eq. (4)

without considering the solid state. Some sample curves of $f_u(\bar{n})$ near $C_0 = 0$ are plotted in Fig. 1(a), which shows a double-well free energy when C_0 is positive, i.e., in the regime of $\epsilon > 1$. The corresponding phase diagram with vapor-liquid coexistence is given in Fig. 1(b), where the critical point locates at $\bar{n} = 0$, $C_0 = 0$ ($\epsilon = 1$). Below the critical point, vapor and liquid are indistinguishable and there is no vapor-liquid coexistence. Above the critical point, vapor-liquid coexistence occurs and the coexistence regime expands with increasing C_0 . Note that this result applies in the absence of solid phase which could become more stable in this parameter regime in the original PFC model.

The vapor-liquid coexistence is affected by the cubic term with nonzero D_0 . Applying the common tangent rule on $f_u(\bar{n})$ in Eq. (4), values of \bar{n} for the vapor and liquid phases in coexistence are given by

$$\bar{n}_{\text{coexist}} = \frac{-D_0 \pm \sqrt{3D_0^2 - 6C_0E_0}}{E_0}. \quad (5)$$

The spinodal densities are determined by $\partial^2 f_u / \partial \bar{n}^2 = 0$, yielding

$$\bar{n}_{\text{spinodal}} = \frac{-D_0 \pm \sqrt{D_0^2 - 2C_0E_0}}{E_0}. \quad (6)$$

The corresponding results are plotted in Fig. 1(c) as a function of D_0 . Introducing D_0 expands the region of vapor-liquid coexistence. For example, in the absence of D_0 the coexistence occurs only when $C_0 > 0$; in contrast, as shown in Fig. 1(c) with $E_0 = -6$, at $D_0 = \pm 3.46$ the coexistence regions is expanded to $C_0 > -1$, i.e., to smaller values of ϵ within the scope of original PFC model.

In short, the above analysis indicates that the vapor-liquid coexistence can be realized within the PFC framework of a single density order parameter when $D_0^2 > 2C_0E_0$ (with $E_0 < 0$), under either large enough C_0 (or ϵ) or large enough $|D_0|$.

B. Conditions for vapor-liquid-solid transitions

With the knowledge of vapor-liquid coexistence given above, we now explore the way to realize vapor-liquid-solid transitions. To simplify the problem and facilitate theoretical analysis, we adopt a one-mode approximation for $n(\mathbf{r})$ of periodic solid phases. For a one-dimensional (1D) stripe phase with amplitude A and wave number q ,

$$n(\mathbf{r}) = \bar{n} + A(e^{iqx} + \text{c.c.}). \quad (7)$$

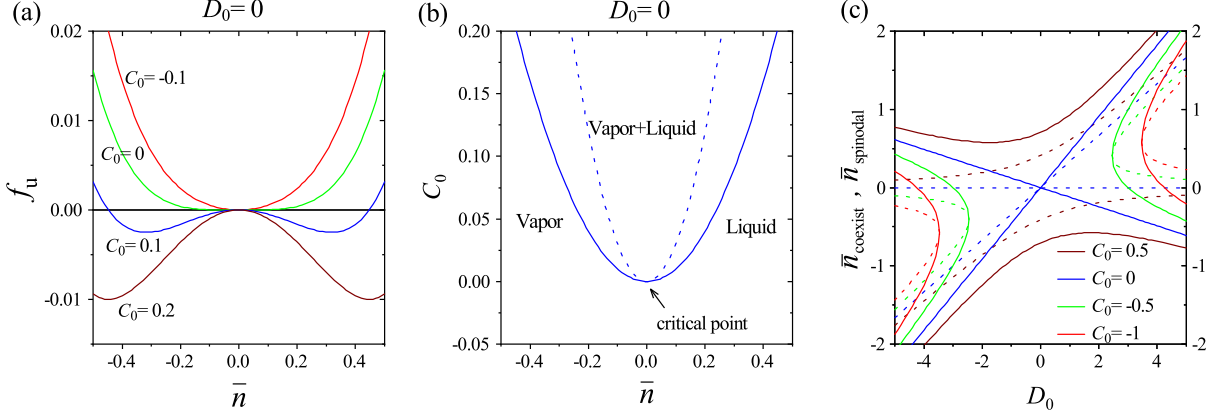


FIG. 1. Coexistence of vapor and liquid phases if not considering the solid state. (a) The free energy density of uniform phase as a function of \bar{n} at different C_0 ($= \epsilon - 1$). (b) The C_0 - \bar{n} phase diagram for vapor and liquid states, where the boundary of vapor-liquid coexistence is plotted as solid lines and the spinodal line is plotted as dashed. $D_0 = 0$ is set in both (a) and (b). (c) The density of vapor-liquid coexistence (\bar{n}_{coexist} , solid curves) or the spinodal density ($\bar{n}_{\text{spinodal}}$, dashed curves) as a function of D_0 at different values of C_0 . Other parameters are $B_0 = 0$ and $E_0 = -6$.

Substituting it into Eq. (3) yields the corresponding free energy density

$$\begin{aligned}
 f_{\text{stripe}}(q, A; \bar{n}) &= -B_0\bar{n} - \frac{1}{2}C_0\bar{n}^2 - \frac{1}{6}D_0\bar{n}^3 - \frac{1}{24}E_0\bar{n}^4 \\
 &- \left[(C_0 - C_2q^2 + C_4q^4) + \frac{1}{3}(3D_0 - 2D_{11}q^2)\bar{n} \right. \\
 &\left. + \frac{1}{12}(6E_0 + E_{1122}q^4)\bar{n}^2 \right] A^2 - \frac{1}{4}(E_0 + E_{1122}q^4)A^4.
 \end{aligned} \tag{8}$$

Note that for simplicity, here we assume $C_6 = 0$ in the free energy as the presence of C_6 term would not affect the basics of vapor-liquid-solid transition sequence. The specific role played by nonzero C_6 will be discussed separately at the beginning of Sec. IV A. Similarly, for a 2D hexagonal or triangular phase the density field is expanded as

$$n(\mathbf{r}) = \bar{n} + A \sum_{\mathbf{q}} (e^{i\mathbf{q}\cdot\mathbf{r}} + \text{c.c.}), \tag{9}$$

where the basic wave vectors $\mathbf{q} = q(1, 0)$, $q(1/2, \sqrt{3}/2)$, and $q(1/2, -\sqrt{3}/2)$. The free energy density is then written by

$$\begin{aligned}
 f_{\text{hex}}(q, A; \bar{n}) &= -B_0\bar{n} - \frac{1}{2}C_0\bar{n}^2 - \frac{1}{6}D_0\bar{n}^3 - \frac{1}{24}E_0\bar{n}^4 \\
 &- 3 \left[(C_0 - C_2q^2 + C_4q^4) + \frac{1}{3}(3D_0 - 2D_{11}q^2)\bar{n} \right. \\
 &\quad \left. + \frac{1}{12}(6E_0 + E_{1122}q^4)\bar{n}^2 \right] A^2 \\
 &- [2(D_0 - D_{11}q^2) + (2E_0 + E_{1122}q^4)]\bar{n} A^3 \\
 &- \frac{15}{4}(E_0 + E_{1122}q^4)A^4.
 \end{aligned} \tag{10}$$

The equilibrium state is determined by minimizing the free energy density, i.e., $\min_{q,A} f(q, A; \bar{n})$ via $\partial f/\partial q = 0$ and $\partial f/\partial A = 0$. The corresponding results of equilibrium free energy density for stripe and hexagonal phases are plotted in Fig. 2 as a function of \bar{n} .

The first row of Eq. (8) or Eq. (10) is identical to that of the uniform phase, either liquid or vapor, given in Eq. (4). To identify the conditions for achieving the vapor-liquid-solid transition sequence as \bar{n} increases, in the following we consider the linear instability of the supercooled or supersaturated uniform phase with respect to the formation of the crystalline state, which is determined by the A^2 term in Eqs. (8) and (10), both being proportional to

$$\begin{aligned}
 \alpha(q, \bar{n}) &= - \left[(C_0 - C_2q^2 + C_4q^4) + \frac{1}{3}(3D_0 - 2D_{11}q^2)\bar{n} \right. \\
 &\quad \left. + \frac{1}{12}(6E_0 + E_{1122}q^4)\bar{n}^2 \right].
 \end{aligned} \tag{11}$$

When $\alpha < 0$, a uniform liquid or vapor phase is linearly unstable under infinitesimal fluctuations and will crystallize spontaneously. To find the minimum of α with respect to q , we solve $\partial\alpha/\partial q = 0$, leading to

$$q^2 = \begin{cases} \frac{6C_2 + 4D_{11}\bar{n}}{12C_4 + E_{1122}\bar{n}^2}, & \text{if } 3C_2 + 2D_{11}\bar{n} < 0, \\ 0, & \text{if } 3C_2 + 2D_{11}\bar{n} \geq 0, \end{cases} \tag{12}$$

where $12C_4 + E_{1122}\bar{n}^2 < 0$ is required to prevent the divergence at large q as can be obtained from Eq. (11). Substituting Eq. (12) into Eq. (11) yields

$$\alpha(\bar{n}) = - \left(C_0 + D_0\bar{n} + \frac{1}{2}E_0\bar{n}^2 \right) + \frac{(3C_2 + 2D_{11}\bar{n})^2}{3(12C_4 + E_{1122}\bar{n}^2)}, \tag{13}$$

for $3C_2 + 2D_{11}\bar{n} < 0$.

If $D_{11} = E_{1122} = 0$ as in the original PFC model, we have $q^2 = C_2/2C_4$ which is independent of \bar{n} , and $C_2 < 0$

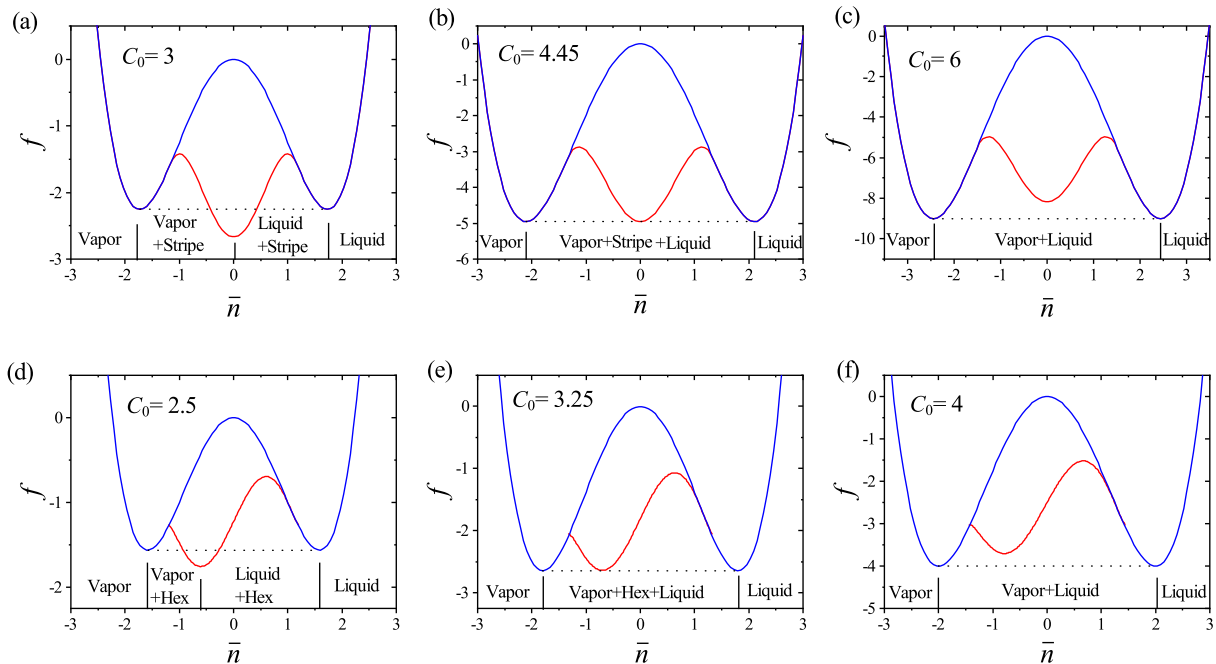


FIG. 2. Equilibrium free energy density of uniform (blue) and solid (red) phases as a function of \bar{n} at different values of C_0 in one-mode approximation, where the solid phase is of (a)–(c) 1D stripe or (d)–(f) 2D hexagonal (Hex) symmetry. The parameters used are $B_0 = C_6 = D_0 = D_{11} = E_{1122} = 0$, $C_2 = -2$, $C_4 = -1$, and $E_0 = -6$.

is needed to enable solid phases. Defining the supercooling or supersaturating density for the occurrence of linear instability by $\alpha(\bar{n}) = 0$, we have

$$\bar{n}_{\text{supercool}}^{(o)} = \frac{-D_0 \pm \sqrt{D_0^2 - 2E_0(C_0 - C_2^2/4C_4)}}{E_0}. \quad (14)$$

A solid phase would be more stable than a uniform phase (vapor or liquid) when \bar{n} lies in between the two values of $\bar{n}_{\text{supercool}}^{(o)}$. Comparing Eq. (14) with Eqs. (5) and (6), it is clear that the midpoint of two $\bar{n}_{\text{supercool}}^{(o)}$ coincides with that of \bar{n}_{coexist} or $\bar{n}_{\text{spinodal}}$ for vapor-liquid phases. Therefore, the stability regime of solid phase is expected to locate in between those of vapor and liquid, and the phase transition sequence is thus vapor-solid-liquid with

the increase of density, consistent with the results of free energy density curves given in Fig. 2 for both 1D and 2D systems. The vapor-solid-liquid coexistence (corresponding to the triple point in phase diagram) can be realized via adjusting model parameters appropriately, as shown in Figs. 2(b) and 2(e). In this case, the density of solid is smaller than that of liquid, mimicking the unusual property of ice vs. water but not the behavior of most other materials. The above analysis hence demonstrates that it is impossible to describe the usual vapor-liquid-solid transition sequence in the original PFC model with $D_{11} = E_{1122} = 0$.

To achieve the usual vapor-liquid-solid transition sequence, we need to consider the effect of nonzero D_{11} . When $E_{1122} = 0$, $\alpha(\bar{n})$ in Eq. (13) keeps its quadratic form of \bar{n} and the linearly unstable condition of $\alpha(\bar{n}) = 0$ is still solvable analytically, yielding

$$\bar{n}_{\text{supercool}} = \frac{-\left(D_0 - \frac{C_2 D_{11}}{3C_4}\right) \pm \sqrt{\left(D_0 - \frac{C_2 D_{11}}{3C_4}\right)^2 - 2\left(E_0 - \frac{2D_{11}^2}{9C_4}\right)\left(C_0 - \frac{C_2^2}{4C_4}\right)}}{E_0 - \frac{2D_{11}^2}{9C_4}}. \quad (15)$$

Now the midpoint of two $\bar{n}_{\text{supercool}}$ values does not coincide with that of \bar{n}_{coexist} or $\bar{n}_{\text{spinodal}}$ anymore. More importantly, when the quadratic coefficient of $\alpha(\bar{n})$ in Eq. (13), i.e., $-E_0/2 + D_{11}^2/9C_4$, is negative, the solid

phase is more stable than the vapor or liquid uniform phase for \bar{n} lying outside the range confined by the two $\bar{n}_{\text{supercool}}$ values, but not in between them as before. This makes it possible to tune the phase stability parameters

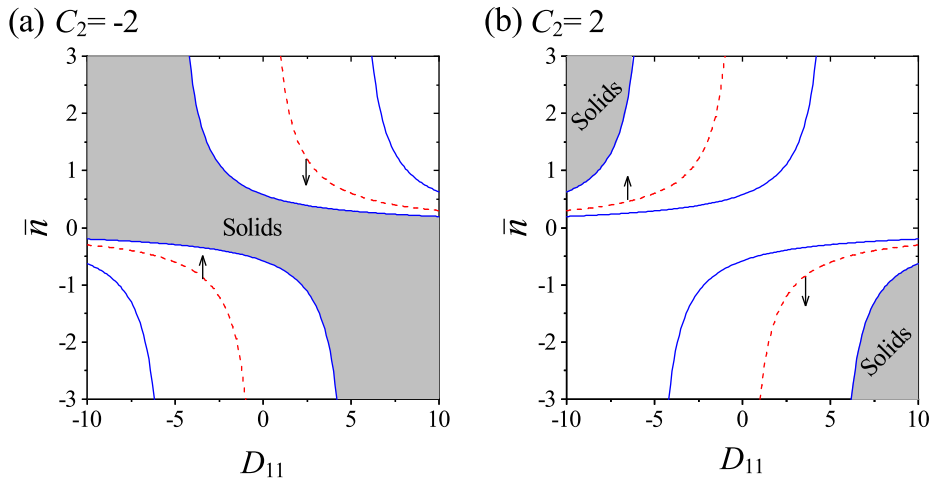


FIG. 3. Variation of $\bar{n}_{\text{supercool}}$ with D_{11} . Calculations are based on Eq. (15) shown as solid curves. The dashed lines correspond to $3C_2 + 2D_{11}\bar{n} = 0$, while arrows point to the region of $3C_2 + 2D_{11}\bar{n} < 0$. Regions for solid phase are shown in shadow. The parameters used are $B_0 = C_6 = D_0 = E_{1122} = C_0 = 0$, $C_4 = -1$, $E_0 = -6$, and (a) $C_2 = -2$, (b) $C_2 = 2$.

such that the density of solid would be higher than that of liquid, i.e., to realize the usual vapor-liquid-solid transition sequence. Some examples are illustrated in Fig. 3, where C_0 is set as 0 to approach the vapor-liquid coexistence, and $D_0 = 0$ is assigned by properly choosing the reference state so that vapor and liquid phases locate at opposite sides of $\bar{n} = 0$ in the parameter space. In such a case, a vapor-liquid-solid transition sequence requires the solid phase to be on the positive side of \bar{n} . However, for $C_2 = -2$ as used in most PFC models, the stability regime for solid always contains the point $\bar{n} = 0$ [see Fig. 3(a)]; i.e., at $\bar{n} = 0$ the solid state is more stable than the uniform phase. This can be easily verified from Eqs. (12) and (13) which show that $q^2 > 0$ and $\alpha(\bar{n}) < 0$ always hold at $\bar{n} = 0$ for any $C_0 \geq 0$ (which is necessary for vapor-liquid coexistence when $D_0 = 0$; see Sec. III A), $C_2 < 0$, and $C_4 < 0$. It is noted that based on Eq. (12), $3C_2 + 2D_{11}\bar{n} < 0$ is needed for the appearance of solid state, giving $C_2 < 0$ in the absence of D_{11} as in previous PFC models. Conversely, with the introducing of nonzero D_{11} , $C_2 < 0$ is no longer obligatory (see also Appendix A). When $C_2 = 2$ [Fig. 3(b)], in the D_{11} - \bar{n} diagram the stability regime for solid phase shrinks as compared to the case of $C_2 = -2$, and locates at large enough $|D_{11}|$. Importantly, the solid phase is not stable near $\bar{n} = 0$, leaving space for vapor-liquid coexistence to occur. As seen in Fig. 3(b), for small enough negative D_{11} the density of solid is higher than that of uniform (vapor or liquid) phase as desired.

The existence of proper vapor-liquid-solid transitions also requires the contribution of the E_{1122} term. The reason is that although nonzero D_{11} enables the stabilization of solid phase at density \bar{n} larger than that of vapor and liquid phases, it overstabilizes the solid phase at very large \bar{n} . Take the stripe phase as an example, for

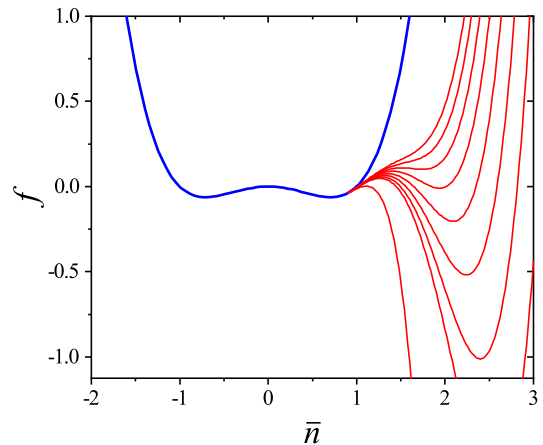


FIG. 4. Equilibrium free energy density of uniform (blue) and stripe (red) phases as a function of \bar{n} in one-mode approximation, for various values of E_{1122} . Result of uniform phase is not affected by E_{1122} , while for stripes the value of free energy density increases with the decrease of E_{1122} , i.e., $E_{1122} = 0, -0.22, -0.24, -0.26, -0.28, -0.30, -0.32, -0.34, -0.36$ (red curves, from bottom to top). Other parameters are $B_0 = C_6 = D_0 = 0$, $C_0 = 0.5$, $C_2 = 2$, $C_4 = -1$, $E_0 = -6$, and $D_{11} = -8$.

which the free energy density at $E_{1122} = 0$ is

$$f_{\text{stripe}}(\bar{n}) = -B_0\bar{n} - \frac{1}{2}C_0\bar{n}^2 - \frac{1}{6}D_0\bar{n}^3 - \frac{1}{24}E_0\bar{n}^4 + \frac{1}{E_0} \left[\frac{(3C_2 + 2D_{11}\bar{n})^2}{18C_4} - \left(C_0 + D_0\bar{n} + \frac{1}{2}E_0\bar{n}^2 \right) \right]^2 \quad (16)$$

when $3C_2 + 2D_{11}\bar{n} < 0$. The value of $f_{\text{stripe}}(\bar{n})$ is dominated by the \bar{n}^4 terms when $\bar{n} \gg 1$. To prevent

$f_{\text{stripe}} \rightarrow -\infty$, it is required that

$$-\frac{1}{24}E_0 + \frac{1}{E_0} \left[\frac{2D_{11}^2}{9C_4} - \frac{E_0}{2} \right]^2 > 0, \quad (17)$$

which however is incompatible with the condition of $-E_0/2 + D_{11}^2/9C_4 < 0$ for the occurrence of vapor-liquid-solid transition sequence as discussed above. Therefore, a negative E_{1122} is necessary to remedy this, as demonstrated in Fig. 4 which shows the increase of f_{stripe} and the avoidance of divergence as E_{1122} becomes more negative.

In the next section we will conduct numerical calculations beyond one-mode approximation to achieve the three-phase coexistence and transition, based on the above theoretical analyses and the conditions identified for the realization of proper vapor-liquid-solid transitions.

IV. NUMERICAL RESULTS

Numerical calculations are conducted through the use of the time-evolution equation

$$\frac{\partial n}{\partial t} = \nabla^2 \frac{\delta \mathcal{F}[n]}{\delta n}, \quad (18)$$

which describes the conserved dynamics of density variation field $n(\mathbf{r}, t)$. Given Eq. (3) for the free energy functional \mathcal{F} of this model, the above dynamic equation is of the explicit form

$$\begin{aligned} \frac{\partial n}{\partial t} = \nabla^2 \left\{ - (C_0 + C_2 \nabla^2 + C_4 \nabla^4 + C_6 \nabla^6) n \right. \\ \left. - \frac{1}{2} D_0 n^2 - \frac{1}{6} D_{11} (2n \nabla^2 n + \nabla^2 n^2) \right. \\ \left. - \frac{1}{6} E_0 n^3 - \frac{1}{12} E_{1122} [n(\nabla^2 n)^2 + \nabla^2 (n^2 \nabla^2 n)] \right\} \quad (19) \end{aligned}$$

It is essentially governed by the diffusive, relaxational dynamics, and the system free energy decreases with time t continuously until it reaches an equilibrium or steady state.

A. Vapor-liquid-solid coexistence and phase diagrams

Our above analyses have demonstrated that the free-energy functional Eq. (3) with $C_6 = 0$ is sufficient in obtaining the vapor-liquid-solid transitions under one-mode approximation. However, when solving the full PFC model via e.g., the dynamical Eq. (18), higher-order modes play a non-neglectable role and could cause undesired disturbances on the phase behavior. To enhance the dynamical stability of the one-mode-like solutions, we introduce the nonzero C_6 term into the two-point direct correlation, which can be used to control the degree of

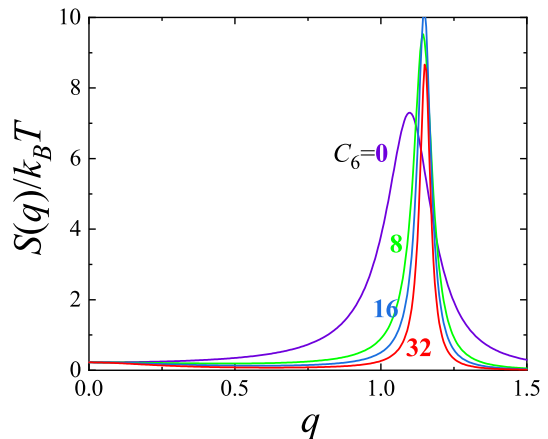


FIG. 5. The fluid-state structure factor $S(q)$ at different values of C_6 , evaluated from the analytic result derived in Appendix A. The curves are plotted with four sets of parameters, including $(C_6, C_2, C_4) = (0, -10.6, -2.88)$, $(8, 3.63, 18.5)$, $(16, 17.8, 39.8)$, and $(32, 46.3, 82.5)$, with other parameters $C_0 = -5.75$, $D_0 = -9$, $E_0 = -6$, $D_{11} = -34.2$, $E_{1122} = -52.1$, and $\bar{n} = -0.15$ remaining the same for each set. Each parameter set would lead to a state of vapor-liquid-solid coexistence under one-mode approximation of 2D hexagonal structure when $\bar{n}_{\text{vapor}} = -2.5$, $\bar{n}_{\text{liquid}} = -0.5$, $\bar{n}_{\text{solid}} = 0$, and $A = 0.2$. As C_6 increases the peak position of $S(q)$ approaches the value $q = 2/\sqrt{3}$ used in one-mode approximation.

contributions from high-order modes on system properties. An example is given in Fig. 5, showing some sample results of equilibrium fluid-state structure factor $S(q)$ (as derived in Appendix A) for different values of C_6 , each of which corresponds to a set of model parameters giving vapor-liquid-solid coexistence. These results indicate that contributions from high-order modes can be effectively suppressed at large C_6 .

With the introduction of nonzero C_6 , we can identify a broad range of parameters that lead to vapor-liquid-solid coexistence in the new PFC model developed here. The general procedure for identifying the corresponding model parameters are described in Appendix B, which needs to be combined with some analytic conditions derived above in Sec. III in the absence of C_6 (particularly $D_0^2 > 2C_0 E_0$, $D_{11} < 0$, and $E_{1122} < 0$). Numerical calculations are needed even in one-mode approximation, with some results presented in Fig. 6. Without loss of generality, in this example we fix the parameters $C_0 = -5.75$, $D_0 = -9$, and $E_0 = -6$ so that vapor-liquid coexistence is found at $\bar{n}_{\text{vapor}} = -2.5$ and $\bar{n}_{\text{liquid}} = -0.5$ from Eq. (5). We then search for all the possible values of C_2 , C_4 , D_{11} , and E_{1122} that give the solution of three-phase coexistence. Results in Fig. 6(a) indicates that the solution exists across a broad range of solid-phase coexistence density \bar{n}_{solid} and amplitude A . [It is interesting to note that in addition to vapor-liquid-solid coexistence (with $\bar{n}_{\text{vapor}} < \bar{n}_{\text{liquid}} < \bar{n}_{\text{solid}}$), the parameter range for the unusual vapor-solid-liquid coexistence

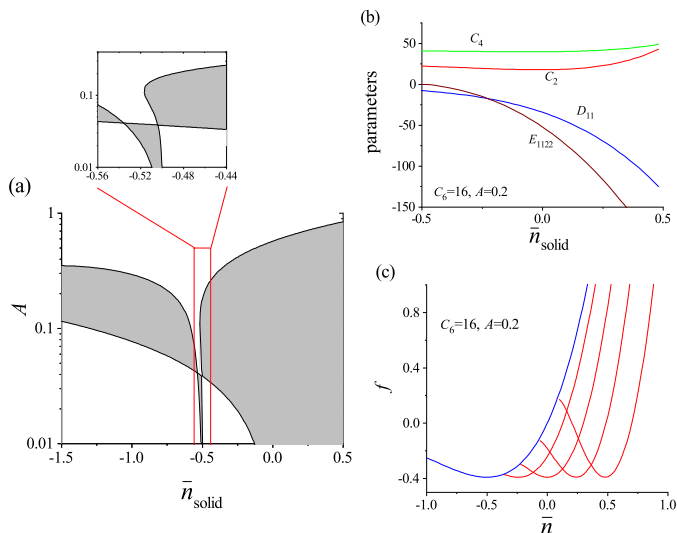


FIG. 6. The broad range of model parameters yielding three-phase coexistence, under the condition of fixed values of $B_0 = -1.875$, $C_0 = -5.75$, $D_0 = -9$, and $E_0 = -6$ such that vapor-liquid coexistence occurs at $\bar{n}_{\text{vapor}} = -2.5$ and $\bar{n}_{\text{liquid}} = -0.5$. (a) Values of solid-phase coexistence density \bar{n}_{solid} and one-mode amplitude A for 2D hexagonal phase that can lead to existence of solutions for vapor-liquid-solid or vapor-solid-liquid coexistence [across all possible combinations of $(C_2, C_4, D_{11}, E_{1122})$], as indicated by the shaded region. The results are generated for $C_6 = 16$, with very similar outcomes for other choices of $C_6 > 0$. (b) The allowed values of parameter set $(C_2, C_4, D_{11}, E_{1122})$ to achieve three-phase coexistence at different \bar{n}_{solid} when $C_6 = 16$ and $A = 0.2$. (c) The free energy density curves of liquid (blue) and solid (red) phases corresponding to four of the parameter sets in (b) that give $\bar{n}_{\text{solid}} = -0.25, 0, 0.25, 0.5$, respectively. The vapor-phase free energy density (not shown here) is minimized at $\bar{n} = -2.5$ that forms a common tangent with these liquid- and solid-phase curves. The procedure of calculations under one-mode approximation is given in Appendix B.

(with $\bar{n}_{\text{vapor}} < \bar{n}_{\text{solid}} < \bar{n}_{\text{liquid}}$) can also be identified in this model, as seen in the part of $-1.5 \leq \bar{n}_{\text{solid}} < -0.5$ in Fig. 6(a).] In other words, at any specific \bar{n}_{solid} within this range the associated values of parameter set $(C_2, C_4, D_{11}, E_{1122})$ can be found to achieve three-phase coexistence [see Fig. 6(b)]. This continuous adjustability of model parameters is demonstrated in an example of Fig. 6(c), where \bar{n}_{solid} is pre-selected from -0.25 to 0.50 and for each of them we can always identify the corresponding combination values of model parameters [given in Fig. 6(b)] to obtain vapor-liquid-solid coexistence.

To obtain accurate values of the solid-phase equilibrium free energy beyond one-mode approximation, we have numerically solved the full dynamical Eq. (18) using a single unit cell with periodic boundary conditions, and calculated the free energy density of its equilibrium, steady state. The initial density field $n(\mathbf{r}, t = 0)$ is set up either from the one-mode solution or from the existing simulation result of close parameter values. In addition,

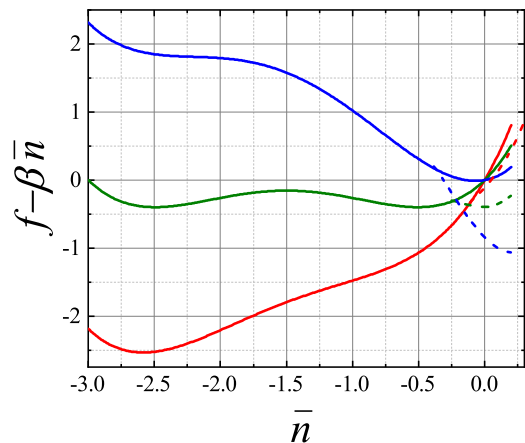


FIG. 7. Free energy density profiles of uniform (solid curves) and 2D hexagonal (dashed) phases at different temperatures $\Delta T = -0.514$ (blue), $\Delta T = 0$ (green), and $\Delta T = 0.486$ (red), using model parameters listed in Table I. Results are obtained from numerical solution of the full dynamical Eq. (18). Here all the free energy density curves have been tilted by a factor of $-\beta\bar{n}$ with $\beta = 2.596$ for a better illustration.

the numerical grid spacings Δx and Δy are varied to determine the equilibrium wave number and thus lattice constant from the minimum point of the corresponding free energy density obtained from simulations at each \bar{n} and temperature. The resulting equilibrium free energy density for solid phase is then lower than that of one-mode approximation (although by a very small degree due to the effect of nonzero C_6 term), and we can slightly adjust the model parameters to achieve the desired phase stability and coexistence.

All the model parameters identified and used in the following full-model numerical calculations are summarized in Table I, where C_0 , C_2 , and C_4 are set to be dependent on an effective temperature ΔT for the coexistence among vapor, liquid, and solid phases (with $\Delta T = 0$ being the triple point temperature). Parameter B_0 for the linear term of the free energy functional is also set as temperature dependent, to produce the proper property of pressure (see below). Examples of the resulting equilibrium profiles of free energy density $f(\bar{n})$ are given in Fig. 7, at three different effective temperatures. At low temperature ($\Delta T = -0.514$) both vapor-liquid and vapor-solid coexistence can be identified from the $f-\bar{n}$ curves through the common tangent construction, while increasing temperature to $\Delta T = 0$ brings the system to a vapor-liquid-solid coexistence as determined by the common tangent of the vapor, liquid, and solid free energy curves. Further increasing the temperature ($\Delta T = 0.486$) excludes vapor-solid coexistence while the separate vapor-liquid and liquid-solid coexistence still remains. At high enough temperature, only liquid-solid coexistence can be found. All these results are consistent with the well-known behavior of the three phases.

The pressure P is also determined by $f(\bar{n})$. In the

TABLE I. Model parameters used in numerical calculations of vapor-liquid-solid transitions. $\Delta T = 0$ corresponds to the triple point temperature.

B_0	C_0	C_2	C_4	C_6	D_0	D_{11}	E_0	E_{1122}
$-4.5 - 3\Delta T$	$-5.764 - \Delta T$	$17.8 + 2\Delta T$	$39.8 - \Delta T$	16	-9	-34.2	-6	-52.1

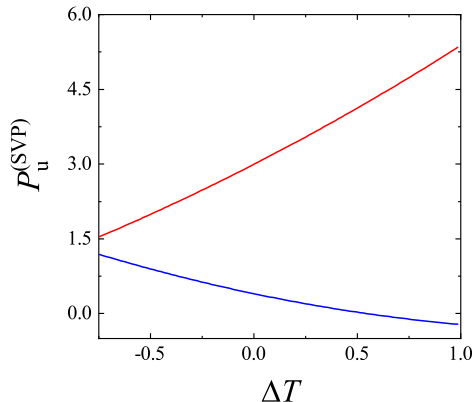


FIG. 8. Saturation vapor pressure at vapor-liquid coexistence as a function of temperature ΔT . Upper red line: $B_0 = -4.5 - 3\Delta T$ as set in Table I; Bottom blue line: $B_0 = 0$.

PFC approach, the quantitative result of pressure depends on the physical interpretation of the density variation field n used in the model⁵². Here we adopt the interpretation that $n = (\rho - \rho_0)/\rho_0$, where ρ is the atomic number density and ρ_0 is a reference-state density. The total number of particles N in the system is kept constant under any deformations of volume V , with $N = \int \rho d\mathbf{r} = \bar{\rho}V = \rho_0(\bar{n} + 1)V$ where $\bar{\rho}$ is the spatial average of $\rho(\mathbf{r})$, leading to $\partial\bar{n}/\partial V = -N/(\rho_0 V^2)$. The equilibrium pressure is hence given by (noting $\mathcal{F} = fV$)

$$P = -\frac{\partial\mathcal{F}}{\partial V} = -f - V\frac{\partial f}{\partial\bar{n}}\frac{\partial\bar{n}}{\partial V} = -f + (\bar{n} + 1)\frac{\partial f}{\partial\bar{n}}. \quad (20)$$

For a solid phase, numerical solution of the full PFC model is required to calculate this pressure P through $f(\bar{n})$ of the equilibrium state. For uniform vapor or liquid phase, we can obtain the analytic expression of P based on Eq. (4) for f , i.e.,

$$P_{\text{uniform}} = -B_0 - \frac{1}{2}C_0(\bar{n}^2 + 2\bar{n}) - \frac{1}{6}D_0(2\bar{n}^3 + 3\bar{n}^2) - \frac{1}{24}E_0(3\bar{n}^4 + 4\bar{n}^3) \quad (21)$$

The saturation vapor pressure $P_u^{(\text{SVP})}$ at vapor-liquid coexistence can be calculated by substituting Eq. (5) for coexistence density into Eq. (21). Some results are depicted in Fig. 8, showing the important role of B_0 on the temperature dependence of P . When $B_0 = 0$ and using values given in Table I for other parameters (bottom blue line in Fig. 8) $P_u^{(\text{SVP})}$ decreases with the increase of temperature ΔT , a behavior that is not correct. The

correct temperature-increasing behavior of $P_u^{(\text{SVP})}$ is obtained only when B_0 is set to be temperature dependent, such as $B_0 = -4.5 - 3\Delta T$ given in Table I (upper red line in Fig. 8).

Based on these information of f and P , we compute the vapor-liquid-solid phase diagrams of the full PFC model using the parameters listed in Table I, as shown in Fig. 9. Following the procedure described above, at each temperature ΔT the equilibrium free energy density f for solid phase is evaluated numerically from simulations of single unit cell for different values of \bar{n} (see some examples in Fig. 7). The resulting f - \bar{n} relations are then used in the common tangent construction described in Appendix B to obtain the temperature-density phase diagram presented in Fig. 9(a). At the same time the corresponding pressure value at phase coexistence densities can be determined from Eqs. (20) and (21) for each ΔT , giving the temperature-pressure phase diagram in Fig. 9(b).

These calculated phase diagrams possess expected properties of vapor-liquid-solid transitions and coexistence. For example, for vapor-solid coexistence at low temperatures (with $\Delta T < 0$) the vapor coexistence density increases with temperature but the solid one decreases, while for liquid-solid coexistence at intermediate and high temperatures ($\Delta T > 0$), both liquid and solid coexistence densities increase with temperature [see Fig. 9(a)]. In addition, both the triple point and critical point are obtained in the temperature-pressure phase diagram [Fig. 9(b)]. We have conducted some numerical simulations to verify the phase behavior identified here, with sample results given below in Sec. IV C. All these results are consistent with experimental phase diagrams of pure materials (e.g., argon) and those of previous computer simulations (such as the Lennard-Jones system).

B. Equilibrium lattice spacing: Effects of thermal expansion and pressure

A drawback of the previous PFC models is the lack of lattice thermal expansion effect, and also the lack of a study of effects of pressure P and density \bar{n} on the lattice constant. For example, in the original PFC model the equilibrium wave number in one-mode approximation is given by $q_{\text{eq}} = \sqrt{C_2/2C_4}$, which is independent of \bar{n} , P , and temperature as C_2 and C_4 were assumed to be temperature independent constants²¹. In this model C_2 and C_4 are set to be dependent on the temperature (see Table I), and with the incorporation of high-order correlations in the model (related to three- and four-point

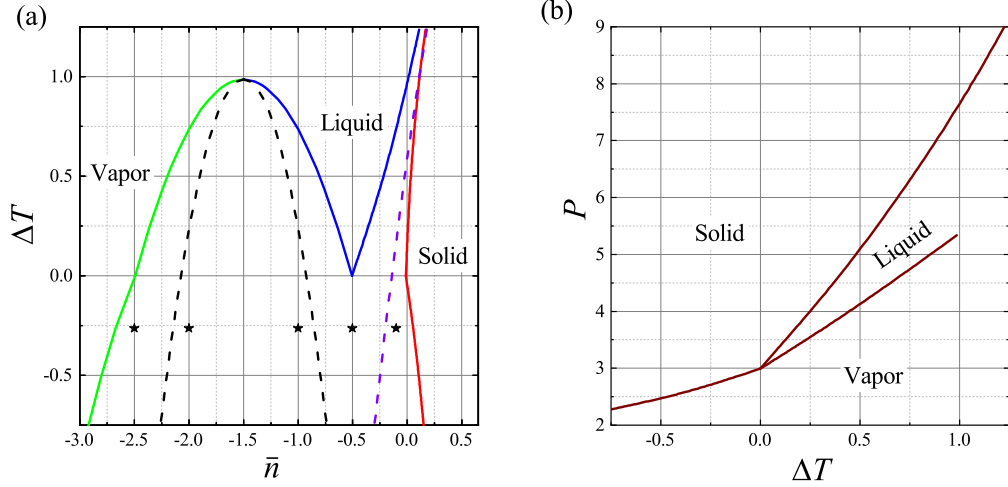


FIG. 9. Vapor-liquid-solid phase diagrams calculated numerically from the full PFC model, where the solid state is of 2D hexagonal phase. (a) Temperature-density phase diagram, where the phase boundaries for vapor, liquid, and solid states are plotted in green, blue, and red, respectively, the vapor-liquid spinodal is plotted as the black dashed curve, and the linear instability of the homogeneous state is indicated by the purple dashed line. Star symbols refer to the 5 parameter locations used in our numerical simulations shown in Fig. 11. (b) Temperature-pressure phase diagram. The model parameters listed in Table I are used.

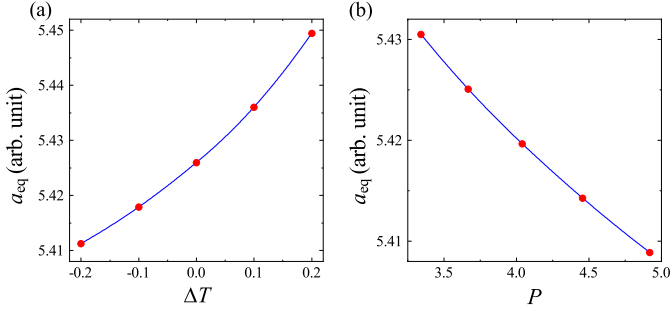


FIG. 10. Thermal and pressure effects on lattice constant. (a) Thermal expansion of equilibrium lattice spacing $a_{\text{eq}} = 2\pi/q_{\text{eq}}$ under a constant pressure $P = 3.87$. (b) The pressure-induced variation of a_{eq} under a constant temperature $\Delta T = 0$. Parameters in Table I for 2D hexagonal phase are used in numerical calculations.

interactions), q_{eq} is affected by \bar{n} and hence pressure P via D_{11} and E_{1122} terms [see e.g., Eq. (12)]. Therefore, both thermal expansion and pressure effects have been incorporated in this three-phase PFC model.

Results of numerical calculations of equilibrium lattice spacing a_{eq} for 2D hexagonal structure are shown in Fig. 10, subjected to variations of temperature and pressure. During the process of equilibrium free energy density and phase diagram calculations described above, q_{eq} has already been determined through free energy minimization at each \bar{n} and ΔT , yielding the corresponding lattice constant $a_{\text{eq}} = 2\pi/q_{\text{eq}}$. For each value of average density \bar{n} , pressure P is calculated numerically based on Eq. (20). Figure 10(a) shows that at a constant value of P , a_{eq} increases with larger temperature ΔT , indicating

a behavior with positive thermal expansion coefficient as in a majority of materials. In addition, when temperature ΔT is kept constant while P is varied, Fig. 10(b) shows that a_{eq} decreases with increasing P , consistent with the compression effect of pressure on the lattice.

C. Dynamical simulations

We have conducted dynamical simulations based on Eq. (18) using the model parameters listed in Table I, to examine the above results of vapor-liquid-solid transitions and coexistence. Our focus is on the regime involving vapor phase at and below the triple point temperature in the phase diagram (i.e., $\Delta T \leq 0$), with some sample results presented in Figs. 11 and 12.

Figure 11 shows five typical scenarios of structural evolution and phase coexistence, with the corresponding parameter values of the initial uniform phase indicated in the temperature-density phase diagram of Fig. 9(a) at $\Delta T = -0.264$. The simulations in Figs. 11(a)–11(d) were initialized from a spatially homogeneous state of density \bar{n}_{uniform} , with a solid seed of 2D hexagonal structure of $\bar{n} = 0.1$ placed at the center, while a random initial condition of $\bar{n} = -0.1$ was set in the whole system of Fig. 11(e). In addition to the spatial structure configurations, the circularly averaged structure factor, diffraction pattern, and the y -averaged density profile along the x direction are presented in Fig. 11 for the final state of simulations. The final state in Figs. 11(a)–11(d) corresponds to equilibrium two-phase coexistence, for which the structure factor shows two peaks, one at small wave number q as caused by the vapor or liquid region while

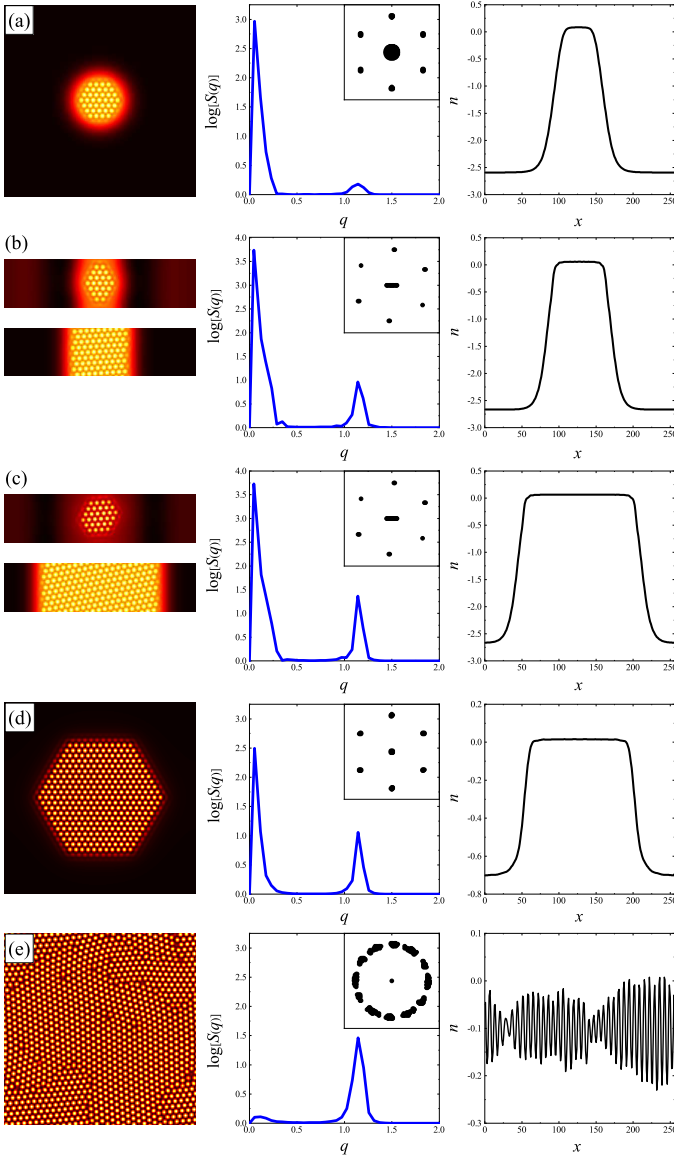


FIG. 11. Sample results from PFC simulations at $\Delta T = -0.264$, corresponding to the locations marked in the phase diagram of Fig. 9(a) below the triple point temperature. They include five characteristic cases for which the initial configuration is set up as a crystalline nucleus of $\bar{n} = 0.1$ and grid size 48×48 embedded in a uniform phase of (a) $\bar{n} = -2.5$, (b) $\bar{n} = -2$, (c) $\bar{n} = -1$, and (d) $\bar{n} = -0.5$, or by (e) a random initial condition of $\bar{n} = -0.1$ in the whole system. Left column: Spatial structure at the steady state of phase coexistence [(a)–(d)] or at the late stage of the polycrystalline state (e). An early-stage configuration having liquid-vapor phase separation is also shown in (b) and (c) for initial \bar{n} within the spinodal. The brighter (darker) regions correspond to higher (lower) values of density field n . Middle column: The corresponding circularly averaged structure factor, with the diffraction pattern shown as inset. Right column: The y -averaged density of the final state across the grid points along the x direction.

the other corresponding to the hexagonal lattice inside the solid grain. For the polycrystalline state in Fig. 11(e), the small- q peak of the structure factor can be attributed to the existence of multiple grains in the sample.

When the initial value of average density \bar{n} locates between the vapor phase boundary and the spinodal curve of the phase diagram, such as $\bar{n}_{\text{uniform}} = -2.5$ in the case of Fig. 11(a), no vapor-liquid separation occurs in the initially homogeneous region and the system equilibrium state is characterized by the coexistence between vapor phase and a stabilized faceted solid grain, as expected. For Fig. 11(b) with $\bar{n}_{\text{uniform}} = -2.0$ and Fig. 11(c) with $\bar{n}_{\text{uniform}} = -1.0$ that are close to two opposite sides of the spinodal boundary, similar results of vapor-solid state are obtained, although with larger equilibrium solid region appearing in the latter case, consistent with the lever rule. Both values of \bar{n}_{uniform} locate within the spinodal regime, so that vapor-liquid phase separation occurs spontaneously at the early stage of system evolution, as can be seen in the top panels of the left column in Figs. 11(b) and 11(c). The liquid-phase region shrinks with time and eventually disappears, while the initial solid grain grows and saturates, leading to an equilibrium state with vapor-solid coexistence as shown in the bottom panels of the left column (see also the averaged density profile given in the right column). When initially $\bar{n}_{\text{uniform}} = -0.5$, lying between the spinodal curve and linear instability line, the final equilibrium state shows a coexistence between liquid region and the embedded faceted solid grain, as seen in Fig. 11(d). Finally, at $\bar{n} = -0.1$ which is beyond the linear instability line, the initial homogeneous state is linearly unstable, leading to the spontaneous formation of the crystalline structure across the system which evolves to a polycrystalline configuration shown in Fig. 11(e). The system consists of various topological defects including dislocations and grain boundaries, resulting in the spatial oscillations of the y -averaged density profile across the x direction as presented in the bottom-right panel of the figure.

To further illustrate the phenomenon of vapor-liquid-solid coexistence, we simulate a system of 2D slab configuration at $\Delta T = 0$, starting with half of the slab occupied by solid phase with $\bar{n} = -0.012$ while the other half by a homogeneous state with $\bar{n} = -1.5$ (at the middle of the spinodal regime), as shown in Fig. 12(a). Through spinodal decomposition, the system spontaneously evolves into a mixture of vapor, liquid, and solid [Fig. 12(b)]. The resulting smoothed average density [Fig. 12(c)] closely matches to that of the equilibrium phase diagram in Fig. 9(a), i.e., $\bar{n} = -2.493$, -0.507 , and -0.012 for vapor, liquid, and solid phases, respectively. It is noted that in this simulated system the solid region is actually of higher energy due to the existing of interfaces and nonzero interfacial energy, and thus shrinks slowly with time during the system evolution.

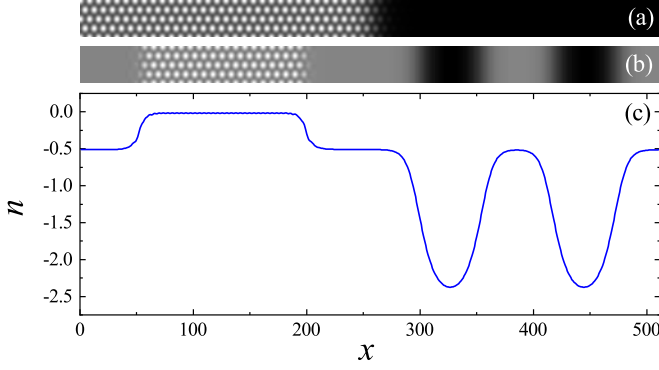


FIG. 12. PFC simulation results of vapor-liquid-solid coexistence at $\Delta T = 0$, using the model parameters given in Table I. (a) The initial state with half of system in solid (with $\bar{n} = -0.012$) and the other half in a uniform state (with $\bar{n} = -1.5$). (b) The time-evolving state with vapor-liquid-solid coexistence. (c) The corresponding y -averaged density along the x direction.

V. SUMMARY

In summary, we have introduced a new PFC model with high-order correlations featuring three- and four-body interactions to examine the transitions and coexistence among vapor, liquid, and crystalline solid phases. The advantage of this model has been demonstrated in terms of its simple form, genericness and flexibility of parameter choices in achieving three-phase coexistence and transitions, including both vapor-liquid-solid and the unusual vapor-solid-liquid transition sequence. Through both theoretical analysis and numerical computation, the conditions of phase coexistence are identified, as well as temperature-density and temperature-pressure phase diagrams incorporating vapor-liquid-solid triple point and vapor-liquid critical point, which qualitatively agree with the well-known results of previous experiments and atomistic simulations. Various scenarios of vapor-solid, liquid-solid, and vapor-liquid-solid coexistence, vapor-liquid phase separation, and structural evolution are verified through dynamical simulations of the model. In addition, several material properties missing in previous PFC models, including temperature dependence of saturation vapor pressure, thermal expansion and compression effect of pressure on lattice constant, can be well produced in this model, with outcomes consistent with the known results. Thus the approach developed here, which well describes the vapor-liquid-solid phase behaviors and the corresponding material properties, can serve as a valuable tool for modeling the material growth and evolution processes including both vapor- and liquid-based and vapor-liquid-solid growth.

Appendix A: Structure factor of the homogeneous state

The structure factor for homogeneous fluids can be determined from a linear analysis of the dynamic equation governing the density field n . In the homogeneous fluid state the density can be decomposed as $n(\mathbf{r}, t) = \bar{n} + \delta n(\mathbf{r}, t)$ with a small fluctuation $\delta n(\mathbf{r}, t)$. Linearizing the dynamical Eq. (18), in Fourier space we get

$$\frac{\partial \delta \hat{n}_{\mathbf{q}}}{\partial t} = -\gamma_{\mathbf{q}} \delta \hat{n}_{\mathbf{q}} + \hat{\eta}_{\mathbf{q}}, \quad (\text{A1})$$

where $\delta \hat{n}_{\mathbf{q}}$ is the Fourier transform of δn , and

$$\gamma_{\mathbf{q}} = q^2 \left[-\left(C_0 + \bar{n} D_0 + \frac{1}{2} \bar{n}^2 E_0 \right) + \left(C_2 + \frac{2}{3} \bar{n} D_{11} \right) q^2 - \left(C_4 + \frac{1}{12} \bar{n}^2 E_{1122} \right) q^4 + C_6 q^6 \right]. \quad (\text{A2})$$

Here we have introduced a noise term $\hat{\eta}_{\mathbf{q}}$, which is the Fourier component of the noise field η satisfying $\langle \eta(\mathbf{r}, t) \rangle = 0$ and $\langle \eta(\mathbf{r}, t) \eta(\mathbf{r}', t') \rangle = -2k_B T \nabla^2 \delta(\mathbf{r} - \mathbf{r}') \delta(t - t')$; thus $\langle \hat{\eta}_{\mathbf{q}}(t) \hat{\eta}_{\mathbf{q}'}^*(t') \rangle = 2k_B T q^2 \delta(\mathbf{q} - \mathbf{q}') \delta(t - t')$.

Following the procedure given in Ref.²⁰, we obtain the solution of Eq. (A1) as

$$\delta \hat{n}_{\mathbf{q}}(t) = e^{-\gamma_{\mathbf{q}} t} \delta \hat{n}_{\mathbf{q}}(0) + e^{-\gamma_{\mathbf{q}} t} \int_0^t ds e^{\gamma_{\mathbf{q}} s} \hat{\eta}_{\mathbf{q}}(s), \quad (\text{A3})$$

and calculate the fluid-state structure factor by

$$\begin{aligned} S(\mathbf{q}, t) &= \langle |\delta \hat{n}_{\mathbf{q}}|^2 \rangle = \langle |\delta \hat{n}_{\mathbf{q}} \delta \hat{n}_{-\mathbf{q}}| \rangle \\ &= e^{-2\gamma_{\mathbf{q}} t} \langle |\delta \hat{n}_{\mathbf{q}}(0)|^2 \rangle \\ &\quad + e^{-2\gamma_{\mathbf{q}} t} \int_0^t ds ds' e^{\gamma_{\mathbf{q}}(s+s')} \langle \hat{\eta}_{\mathbf{q}}(s) \hat{\eta}_{-\mathbf{q}}(s') \rangle \\ &= e^{-2\gamma_{\mathbf{q}} t} S(\mathbf{q}, 0) + \frac{k_B T q^2}{\gamma_{\mathbf{q}}} (1 - e^{-2\gamma_{\mathbf{q}} t}). \end{aligned} \quad (\text{A4})$$

The equilibrium fluid-state structure factor is defined by $S(\mathbf{q}) = S(\mathbf{q}, t \rightarrow \infty)$, yielding

$$S(q) = \frac{k_B T q^2}{\gamma_{\mathbf{q}}} = \frac{k_B T}{-(C'_0 - C'_2 q^2 + C'_4 q^4 - C'_6 q^6)}, \quad (\text{A5})$$

where

$$\begin{aligned} C'_0 &= C_0 + \bar{n} D_0 + \frac{1}{2} \bar{n}^2 E_0, & C'_2 &= C_2 + \frac{2}{3} \bar{n} D_{11}, \\ C'_4 &= C_4 + \frac{1}{12} \bar{n}^2 E_{1122}, & C'_6 &= C_6. \end{aligned} \quad (\text{A6})$$

Appendix B: Phase coexistence and model parameters selection

In this appendix we show the procedure of identifying three-phase coexistence in this PFC model and how

to choose the corresponding model parameters. According to the common tangent rule, in the equilibrium state the coexistence between any two phases is determined by equal chemical potential μ_n and equal pressure P_n , i.e.,

$$\frac{\partial f}{\partial \bar{n}} \Big|_1 = \frac{\partial f}{\partial \bar{n}} \Big|_2 = \mu_n$$

$$f_1 - \mu_n \bar{n}_1 = f_2 - \mu_n \bar{n}_2 = -P_n, \quad (\text{B1})$$

giving coexistence densities \bar{n}_1 and \bar{n}_2 for phase 1 and 2, respectively. [Note that $P_n = P - \mu_n$ if compared to Eq. (20) for pressure P obtained through density $\bar{\rho}$.]

In this PFC model the free energy density for uniform phase, either vapor (f_{vapor}) or liquid (f_{liquid}), is known from Eq. (4), and the exact solution of coexistence densities \bar{n}_{vapor} and \bar{n}_{liquid} is given by Eq. (5). Thus from Eq. (B1) we can get the value of $\mu_n = (f_{\text{liquid}} - f_{\text{vapor}})/(\bar{n}_{\text{liquid}} - \bar{n}_{\text{vapor}})$ from vapor-liquid coexistence, and the following conditions governing the vapor-liquid-solid coexistence

$$\frac{\partial f_{\text{solid}}}{\partial \bar{n}} \Big|_{\bar{n}_{\text{solid}}} = \mu_n = \frac{f_{\text{liquid}} - f_{\text{vapor}}}{\bar{n}_{\text{liquid}} - \bar{n}_{\text{vapor}}}, \quad (\text{B2})$$

$$f_{\text{solid}} = f_{\text{liquid}} + \frac{(\bar{n}_{\text{solid}} - \bar{n}_{\text{liquid}})(f_{\text{liquid}} - f_{\text{vapor}})}{\bar{n}_{\text{liquid}} - \bar{n}_{\text{vapor}}} \quad (\text{B3})$$

For the full model, the solid-state free energy density f_{solid} is calculated from the steady state of the numerical solution of dynamical Eq. (18) for a single-crystal unit cell (see Sec. IV A), while phase coexistence is determined by the common tangent construction described above, given the known results of coexisting vapor and liquid phases in Eqs. (4) and (5).

There are many adjustable parameters in the model, including B_0 , $C_{j=0,2,4,6}$, D_0 , E_0 , D_{11} , and E_{1122} . For simplicity, we first fix the values of B_0 , C_0 , D_0 , and E_0 so that the properties of vapor and liquid phases are predetermined, such as the coexistence densities \bar{n}_{vapor} and \bar{n}_{liquid} , the resulting f_{vapor} and f_{liquid} , and saturation vapor pressure (see Fig. 8). Value of C_6 is also chosen in advance based on its effect on high-order modes (see e.g.,

Fig. 5). We then have only four parameters C_2 , C_4 , D_{11} , and E_{1122} left to be determined, to satisfy the conditions of three-phase coexistence.

We first follow this procedure with the use of one-mode approximation for solid phase to determine all the model parameters, and then slightly adjust them (to account for the discrepancy between one-mode and full-model results) to obtain phase coexistence and phase diagrams from numerical calculations of the full PFC model. The one-mode free energy density f_{solid} is given by Eq. (8) for 1D stripe and by Eq. (10) for 2D hexagonal phase, respectively. Its equilibrium state with minimum free energy is obtained by solving

$$\frac{\partial f_{\text{solid}}}{\partial A} = 0, \quad \frac{\partial f_{\text{solid}}}{\partial q} = 0. \quad (\text{B4})$$

We thus have four equations in Eqs. (B2)–(B4) to be solved numerically for seven unknown variables C_2 , C_4 , D_{11} , E_{1122} , A , q , and \bar{n}_{solid} in one-mode approximation. To identify the allowed values of model parameters C_2 , C_4 , D_{11} , and E_{1122} yielding three-phase coexistence, we solve these equations under specific values of A , \bar{n}_{solid} , and q (fixed as $2/\sqrt{3}$ here in 2D one-mode expansion at the triple point) that can lead to the existence of solution. The corresponding results are presented in Fig. 6.

ACKNOWLEDGMENTS

Z.R.L. acknowledges support from the National Natural Science Foundation of China (Grant No. 21773002). Z.-F.H. acknowledges support from the U.S. National Science Foundation under Grant No. DMR-1609625. W.D. acknowledges support from the National Natural Science Foundation of China (Grant No. 51788104), the Ministry of Science and Technology of China (Grant No. 2016YFA0301001), and the Beijing Advanced Innovation Center for Materials Genome Engineering.

* LiuZhiRong@pku.edu.cn

† huang@wayne.edu

‡ duanw@tsinghua.edu.cn

¹ J. Stangl, V. Holy, and G. Bauer, Structural properties of self-organized semiconductor nanostructures, *Rev. Mod. Phys.* **76**, 725 (2004).

² J.-N. Aqua, I. Berbezier, L. Favre, T. Frisch, and A. Ronda, Growth and self-organization of SiGe nanostructures, *Phys. Rep.* **522**, 59 (2013).

³ O. V. Yazyev and Y. P. Chen, Polycrystalline graphene and other two-dimensional materials, *Nat. Nanotechnol.* **9**, 755 (2014).

⁴ X. Liu and M. C. Hersam, Interface characterization and control of 2d materials and heterostructures, *Adv. Mater.* **30**, 1801586 (2018).

⁵ S. M. Kim, A. Hsu, P. T. Araujo, Y.-H. Lee, T. Palacios, M. Dresselhaus, J.-C. Idrobo, K. K. Kim, and J. Kong, Synthesis of patched or stacked graphene and hBN flakes: A route to hybrid structure discovery, *Nano Lett.* **13**, 993 (2013).

⁶ J. B. Hannon, S. Kodambaka, F. M. Ross, and R. M. Tromp, The influence of the surface migration of gold on the growth of silicon nanowires, *Nature* **440**, 69 (2006).

⁷ P. D. Yang, H. Q. Yan, R. R. S. Mao, J. Johnson, R. Saykally, N. Morris, J. Pham, R. R. He, and H.-J. Choi, Controlled growth of ZnO nanowires and their optical properties, *Adv. Funct. Mater.* **12**, 323 (2002).

⁸ L. Meng, Q. Sun, J. Wang, and F. Ding, Molecular dynamics simulation of chemical vapor deposition graphene growth on Ni(111) surface, *J. Phys. Chem. C* **116**, 6097

- (2012).
- ⁹ Z. Xu, G. Zhao, L. Qiu, X. Zhang, G. Qiao, and F. Ding, Molecular dynamics simulation of graphene sinking during chemical vapor deposition growth on semi-molten Cu substrate, *npj Comput. Mater.* **6**, 14 (2020).
 - ¹⁰ T. Haxhimali, D. Buta, M. Asta, P. W. Voorhees, and J. J. Hoyt, Size-dependent nucleation kinetics at nonplanar nanowire growth interfaces, *Phys. Rev. E* **80**, 050601(R) (2009).
 - ¹¹ H. Wang, L. A. Zepeda-Ruiz, G. H. Gilmer, and M. Upmanyu, Atomistics of vapour-liquid-solid nanowire growth, *Nat. Commun.* **4**, 1956 (2013).
 - ¹² L. Q. Chen, Phase-field models for microstructure evolution, *Annu. Rev. Mater. Sci.* **32**, 113 (2002).
 - ¹³ W. J. Boettinger, J. A. Warren, C. Beckermann, and A. Karma, Phase-field simulation of solidification, *Annu. Rev. Mater. Sci.* **32**, 163 (2002).
 - ¹⁴ Y. Z. Wang and J. Li, Phase field modeling of defects and deformation, *Acta Mater.* **58**, 1212 (2010).
 - ¹⁵ E. J. Schwalbach, S. H. Davis, P. W. Voorhees, D. Wheeler, and J. A. Warren, Liquid droplet dynamics and complex morphologies in vapor-liquid-solid nanowire growth, *J. Mater. Res.* **26**, 2186 (2011).
 - ¹⁶ Y. Wang, P. C. McIntyre, and W. Cai, Phase field model for morphological transition in nanowire vapor-liquid-solid growth, *Cryst. Growth Des.* **17**, 2211 (2017).
 - ¹⁷ N. Wang, M. Upmanyu, and A. Karma, Phase-field model of vapor-liquid-solid nanowire growth, *Phys. Rev. Materials* **2**, 033402 (2018).
 - ¹⁸ J. Zhuang, W. Zhao, L. Qiu, J. Xin, J. Dong, and F. Ding, Morphology evolution of graphene during chemical vapor deposition growth: A phase-field theory simulation, *J. Phys. Chem. C* **123**, 9902 (2019).
 - ¹⁹ K. R. Elder, M. Katakowski, M. Haataja, and M. Grant, Modeling elasticity in crystal growth, *Phys. Rev. Lett.* **88**, 245701 (2002).
 - ²⁰ K. R. Elder and M. Grant, Modeling elastic and plastic deformations in nonequilibrium processing using phase field crystals, *Phys. Rev. E* **70**, 051605 (2004).
 - ²¹ K. R. Elder, N. Provatas, J. Berry, P. Stefanovic, and M. Grant, Phase field crystal modeling and classical density functional theory of freezing, *Phys. Rev. B* **75**, 064107 (2007).
 - ²² S. van Teeffelen, R. Backofen, A. Voigt, and H. Löwen, Derivation of the phase-field-crystal model for colloidal solidification, *Phys. Rev. E* **79**, 051404 (2009).
 - ²³ A. J. Archer, M. J. Robbins, U. Thiele, and E. Knobloch, Solidification fronts in supercooled liquids: How rapid fronts can lead to disordered glassy solids, *Phys. Rev. E* **86**, 031603 (2012).
 - ²⁴ D. Taha, S. R. Dlamini, S. K. Mkhonta, K. R. Elder, and Z.-F. Huang, Phase ordering, transformation, and grain growth of two-dimensional binary colloidal crystals: A phase field crystal modeling, *Phys. Rev. Mater.* **3**, 095603 (2019).
 - ²⁵ Z.-F. Huang and K. R. Elder, Mesoscopic and microscopic modeling of island formation in strained film epitaxy, *Phys. Rev. Lett.* **101**, 158701 (2008).
 - ²⁶ K.-A. Wu and P. W. Voorhees, Stress-induced morphological instabilities at the nanoscale examined using the phase field crystal approach, *Phys. Rev. B* **80**, 125408 (2009).
 - ²⁷ G. Tegze, L. Granásy, G. I. Tóth, F. Podmaniczky, A. Jaatinen, T. Ala-Nissila, and T. Pusztai, Diffusion-controlled anisotropic growth of stable and metastable crystal polymorphs in the phase-field crystal model, *Phys. Rev. Lett.* **103**, 035702 (2009).
 - ²⁸ S. Tang, Y.-M. Yu, J. Wang, J. Li, Z. Wang, Y. Guo, and Y. Zhou, Phase-field-crystal simulation of nonequilibrium crystal growth, *Phys. Rev. E* **89**, 012405 (2014).
 - ²⁹ P. Y. Chan, G. Tsekenis, J. Dantzig, K. A. Dahmen, and N. Goldenfeld, Plasticity and dislocation dynamics in a phase field crystal model, *Phys. Rev. Lett.* **105**, 015502 (2010).
 - ³⁰ J. Berry, N. Provatas, J. Rottler, and C. W. Sinclair, Phase field crystal modeling as a unified atomistic approach to defect dynamics, *Phys. Rev. B* **89**, 214117 (2014).
 - ³¹ A. Skaugen, L. Angheluta, and J. Viñals, Dislocation dynamics and crystal plasticity in the phase-field crystal model, *Phys. Rev. B* **97**, 054113 (2018).
 - ³² A. Skaugen, L. Angheluta, and J. Viñals, Separation of elastic and plastic timescales in a phase field crystal model, *Phys. Rev. Lett.* **121**, 255501 (2018).
 - ³³ M. Salvalaglio, L. Angheluta, Z.-F. Huang, A. Voigt, K. R. Elder, and J. Viñals, A coarse-grained phase-field crystal model of plastic motion, *J. Mech. Phys. Solids* **137**, 103856 (2020).
 - ³⁴ D. L. Olmsted, D. Buta, A. Adland, S. M. Foiles, M. Asta, and A. Karma, Dislocation-pairing transitions in hot grain boundaries, *Phys. Rev. Lett.* **106**, 046101 (2011).
 - ³⁵ D. Taha, S. K. Mkhonta, K. R. Elder, and Z.-F. Huang, Grain boundary structures and collective dynamics of inversion domains in binary two-dimensional materials, *Phys. Rev. Lett.* **118**, 255501 (2017).
 - ³⁶ M. Salvalaglio, R. Backofen, K. R. Elder, and A. Voigt, Defects at grain boundaries: A coarse-grained, three-dimensional description by the amplitude expansion of the phase-field crystal model, *Phys. Rev. Mater.* **2**, 053804 (2018).
 - ³⁷ W. Zhou, J. Wang, B. Lin, Z. Wang, J. Li, and Z.-F. Huang, Yielding and jerky plasticity of tilt grain boundaries in high-temperature graphene, *Carbon* **153**, 242 (2019).
 - ³⁸ C. V. Achim, M. Schmiedeberg, and H. Löwen, Growth modes of quasicrystals, *Phys. Rev. Lett.* **112**, 255501 (2014).
 - ³⁹ P. Subramanian, A. J. Archer, E. Knobloch, and A. M. Rucklidge, Three-dimensional icosahedral phase field quasicrystal, *Phys. Rev. Lett.* **117**, 075501 (2016).
 - ⁴⁰ P. Hirvonen, V. Heinonen, H. Dong, Z. Fan, K. R. Elder, and T. Ala-Nissila, Phase-field crystal model for heterostructures, *Phys. Rev. B* **100**, 165412 (2019).
 - ⁴¹ M. Greenwood, N. Provatas, and J. Rottler, Free energy functionals for efficient phase field crystal modeling of structural phase transformations, *Phys. Rev. Lett.* **105**, 045702 (2010).
 - ⁴² A. Jaatinen and T. Ala-Nissila, Extended phase diagram of the three-dimensional phase field crystal model, *J. Phys.: Condens. Matter* **22**, 205402 (2010).
 - ⁴³ V. W. L. Chan, N. Pisutha-Arnond, and K. Thornton, Phase-field crystal model for a diamond-cubic structure, *Phys. Rev. E* **91**, 053305 (2015).
 - ⁴⁴ S. K. Mkhonta, K. R. Elder, and Z.-F. Huang, Exploring the complex world of two-dimensional ordering with three modes, *Phys. Rev. Lett.* **111**, 035501 (2013).
 - ⁴⁵ S. K. Mkhonta, K. R. Elder, and Z.-F. Huang, Emergence of chirality from isotropic interactions of three length scales, *Phys. Rev. Lett.* **116**, 205502 (2016).
 - ⁴⁶ K.-A. Wu, M. Plapp, and P. W. Voorhees, Controlling

- crystal symmetries in phase-field crystal models, *J. Phys.: Condens. Matter* **22**, 364102 (2010).
- ⁴⁷ E. Alster, D. Montiel, K. Thornton, and P. W. Voorhees, Simulating complex crystal structures using the phase-field crystal model, *Phys. Rev. Materials* **1**, 060801 (2017).
- ⁴⁸ M. Seymour and N. Provatas, Structural phase field crystal approach for modeling graphene and other two-dimensional structures, *Phys. Rev. B* **93**, 035447 (2016).
- ⁴⁹ Z.-L. Wang, Z. R. Liu, and Z.-F. Huang, Angle-adjustable density field formulation for the modeling of crystalline microstructure, *Phys. Rev. B* **97**, 180102(R) (2018).
- ⁵⁰ E. J. Schwalbach, J. A. Warren, K.-A. Wu, and P. W. Voorhees, Phase-field crystal model with a vapor phase, *Phys. Rev. E* **88**, 023306 (2013).
- ⁵¹ G. Kocher and N. Provatas, New density functional approach for solid-liquid-vapor transitions in pure materials, *Phys. Rev. Lett.* **114**, 155501 (2015).
- ⁵² Z.-L. Wang, Z.-F. Huang, and Z. R. Liu, Elastic constants of stressed and unstressed materials in the phase-field crystal model, *Phys. Rev. B* **97**, 144112 (2018).